HELIOS Benchmark Calculation:
Diffusion and Multi-Angle Radiation Transport Models

In *HELIOS*, options for modeling radiation transport include:

- flux-limited, multi-group radiation diffusion (planar, cylindrical, and spherical geometries);
- multi-angle short-characteristics (planar and spherical geometries).

Tabulated multi-group opacities can be used for either of the above radiation transport models. When the inline collisional-radiative atomic kinetics modeling is used in *HELIOS-CR*, the multi-angle short-characteristics model is utilized.

While the multi-angle short-characteristics method is often more accurate than the diffusion approximation, particularly for relatively low-Z materials in laboratory plasma experiments, this method is time-independent. Therefore, the time-dependent diffusion model may be better suited for the systems in which the radiation fields vary extremely rapidly.

In this memo, as an illustration of the benchmarking of the radiation transport algorithms, the results of *HELIOS* calculations are compared with analytic solutions. In the latter part of this memo, results are shown for example applications involving the propagation of radiation through Au and CH planar slabs.

Benchmarks

Benchmark 1. Steady-State Planar Cases

For this benchmark problem, a radiation source is applied to an inner boundary of a uniform purely scattering plasma slab. Opacities are assumed to be constant and independent of photon energy; the plasma is not allowed to move; and radiation heating and cooling rates are neglected.

In this case, the diffusion equation reduces to:

$$\frac{\partial E}{\partial t} = c\frac{\partial}{\partial r} D \frac{\partial E}{\partial r} - c\sigma E + 4\pi S ,$$

and the analytic solution for this steady-state problem can be written as:

$$T_r(x) = T_0 \left(\frac{1}{2} \; \frac{\left(\frac{1}{2}+D\lambda\right)e^{\lambda(X-x)} - \left(\frac{1}{2}-D\lambda\right)e^{-\lambda(X-x)}}{\left(\frac{1}{2}+D\lambda\right)^2 e^{\lambda X} - \left(\frac{1}{2}-D\lambda\right)^2 e^{-\lambda X}} \right)^{1/4} .$$

Here, E is the intensity of the radiation field, c is the speed of light, D is the diffusion coefficient, σ is the plasma opacity, S is the source function, T_r is the radiation temperature, T_0 is the temperature of incident radiation, λ is the inverse diffusion length, and X is the plasma width.

The radiation temperature at every point in space is defined as:

$$T_r = \left(\frac{cE}{4\sigma_{SB}} \right)^{1/4},$$

where σ_{SB} is the Stephan-Boltzmann constant. The default flux limiter in *HELIOS* is based on Larsen formalism, where the diffusion coefficient can be written as:

$$D = \left[(3\sigma)^n + \left(\frac{1}{E} \left| \frac{\partial E}{\partial r} \right| \right)^n \right]^{-1/n},$$

with $n = 2$. Without the flux limiter, the diffusion coefficient reduces to $1/3\sigma$. The inverse diffusion length is defined as follows:

$$\lambda = \sqrt{\frac{\sigma}{D}} = \sqrt{3}\ \sigma .$$

For the short-characteristics:

$$T_r(x) = T_0 \left(\frac{1}{2} E_2(\sigma x) \right)^{1/4},$$

where $E_2(x)$ belongs to a family of exponential integrals,

$$E_n(x) = \int_1^\infty \frac{e^{-x\omega}}{\omega^n} d\omega .$$

Results from *HELIOS* calculations are compared with analytic solutions in Figure 1. Results are shown for opacity parameter values of $\sigma = 1\ cm^{-1}$ (left) and $\sigma = 10\ cm^{-1}$ (right). Calculations utilizing the multi-angle short characteristics model were run using 5 angles. Using this model, the results from *HELIOS* are seen to compare favorably with the analytic solutions. Simulation results computed using the diffusion model with flux limiting and without flux limiting are represented by the green and red curves, respectively. Note that the analytic solution for this benchmark diffusion case does not include flux limiting. Again, it is seen that the diffusion results from *HELIOS* are in very good agreement with the analytic solution.

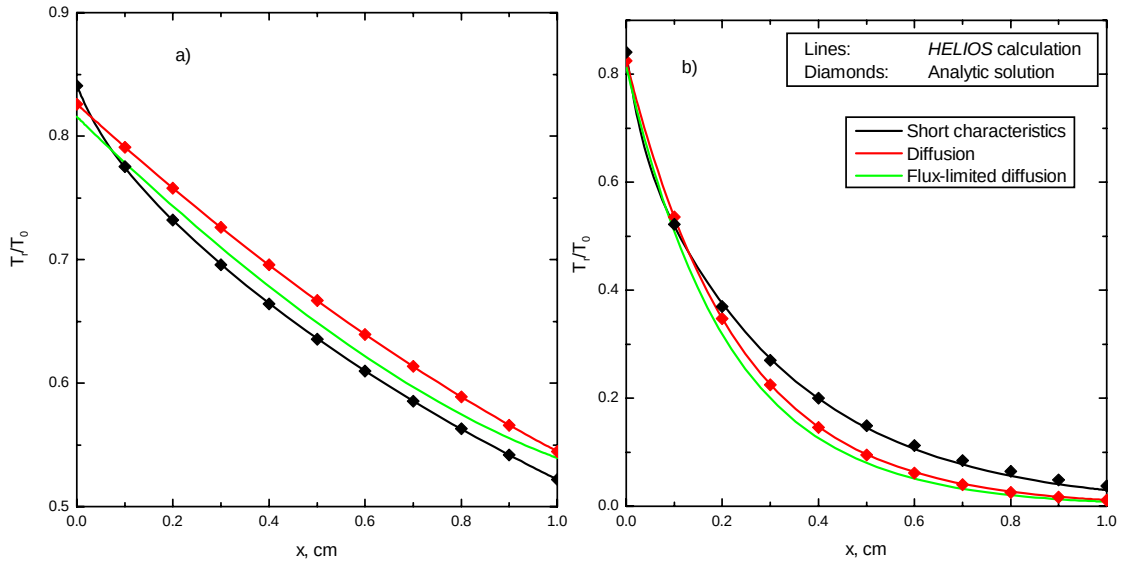

Figure 1. Comparison between planar analytic solutions and HELIOS results using the multi-angle short characteristics model (black), the diffusion model (red), and the flux-limited diffusion model (green). Results are shown for σ = 1 cm^{-1} in the left plot, and σ = 10 cm^{-1} in the right plot. Data for the analytic solutions are represented by diamonds. Note that the analytic solution for diffusion does not include flux limiting.

Benchmark 2. Planar Marshak Wave Simulations

Assumptions for this benchmark case are the same as in the previous example, with the exception of the radiation field being coupled to the plasma (Su and Olson, JQSRT **56**, 337 (1996)). Here, the plasma thermal conductivity is neglected, and the plasma specific heat has an analytic dependence on temperature given by: $c_v = \alpha T^3$. Details of the analytic solutions are rather involved and will not be presented here. For this calculation we have chosen the specific heat coefficient α to be 160 σ_{SB}/c, and the opacity, σ, to be 0.558 cm^{-1}. The solutions for the radiation temperature T_r, and the plasma temperature T_p are presented in terms of a dimensionless length:

$$l = \sqrt{3}\sigma x\,,$$

and time:

$$\tau = \frac{16\sigma_{SB}\sigma}{\alpha}t\,.$$

In this problem, an isotropic radiation field from the boundary source penetrates and heats the plasma. The plasma then starts radiating at the local plasma temperature. The two resulting well-defined wave fronts penetrate deep into the plasma, and, at late times, exhibit virtually identical propagation characteristics.

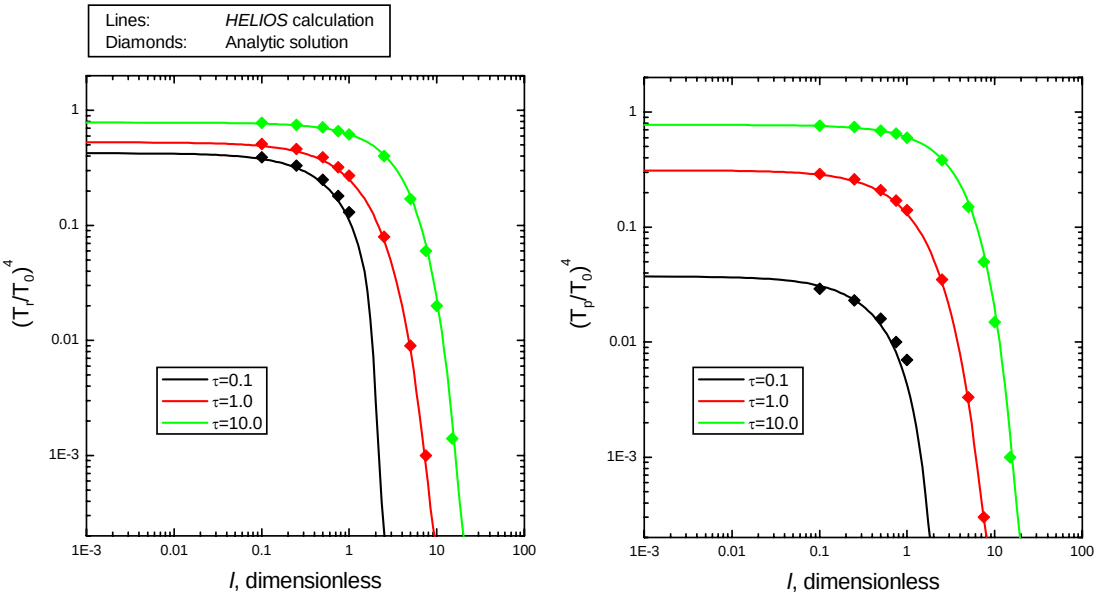

Figure 2. Comparison between planar analytic solutions and HELIOS calculations at dimensionless times of $\tau = 0.1$, 1.0, and 10.0. Left: spatial distribution of radiation temperatures. Right: spatial distribution of plasma temperatures.

In Figure 2, results from *HELIOS* calculations using the time-dependent diffusion model with flux limiting are compared with analytic solutions at dimensionless times of $\tau = 0.1$, 1.0, and 10.0. Radiation temperatures are shown at the left and plasma temperatures are shown at the right. Note that at late times ($\tau >> 1$), the radiation temperature and plasma temperature profiles are nearly the same. The *HELIOS* results show good agreement with the analytic solutions at all times.

Benchmark 3. Steady-State Spherical Cases

For this benchmark problem, a radiation source is applied to an outer boundary of a uniform spherical plasma. As in Benchmark 1, opacities are assumed to be constant and independent of photon energy; the plasma is not allowed to move; and radiation heating and cooling rates are neglected. In spherical geometry, the analytic solution has the following form:

$$T_r(r) = T_0 \left[\frac{1}{2} \frac{R}{\frac{1}{2}\sinh(\lambda R) + D\left(\lambda \cosh(\lambda R) - \frac{\sinh(\lambda R)}{R}\right)} \frac{\sinh(\lambda r)}{r} \right]^{1/4},$$

where r is the radial coordinate, and R is the coordinate at which the radiation source is applied.

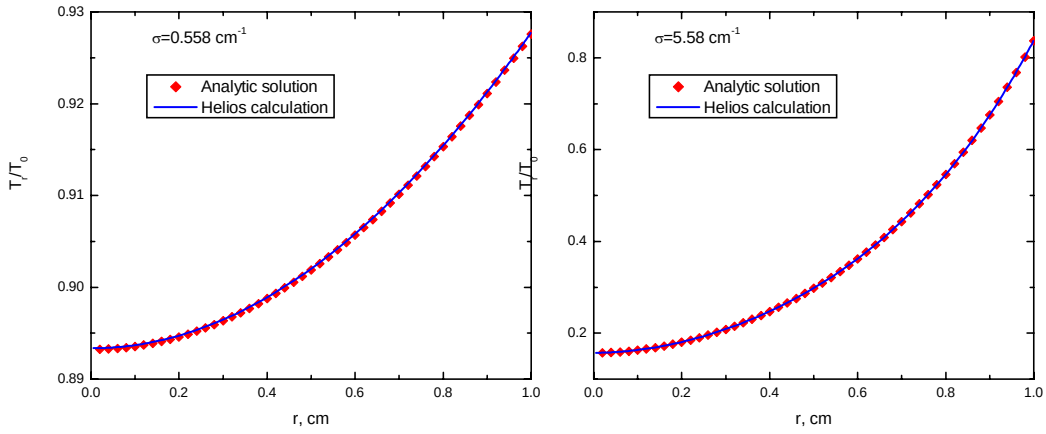

Figure 3. Comparison between steady-state analytic solutions (red symbols) and HELIOS diffusion model results (blue curve) for a uniform spherical plasma. Results are shown for σ = 0.558 cm^{-1} in the left plot, and σ = 5.58 cm^{-1} in the right plot. Note that the analytic solution for diffusion does not include flux limiting.

Figure 3 compares analytic and numeric solutions for R = 1 cm and σ = 0.558 cm^{-1} (left) and 5.58 cm^{-1} (right).

Benchmark 4. Steady-State Cylindrical Cases

Using the same assumptions as the planar and spherical cases (above), the solution for cylindrical geometry can be written in terms of modified Bessel functions of the first kind I:

$$T_r(r) = T_0 \left[\frac{1}{2} \frac{I_0(\lambda r)}{\frac{1}{2} I_0(\lambda R) + D\lambda I_1(\lambda R)} \right]^{1/4} .$$

where r is the radial coordinate, R is the coordinate at which the radiation source is applied, and I_0 and I_1 are modified Bessel functions (see, *e.g.*, Abramowitz and Stegun, Handbook of Mathematical Functions, Dover, 1965).

Figure 4 compares analytic and numeric solutions for R = 1 cm and σ = 0.558 cm^{-1} (left) and 5.58 cm^{-1} (right). As in the planar and spherical cases, agreement between HELIOS and the analytical solutions is very good.

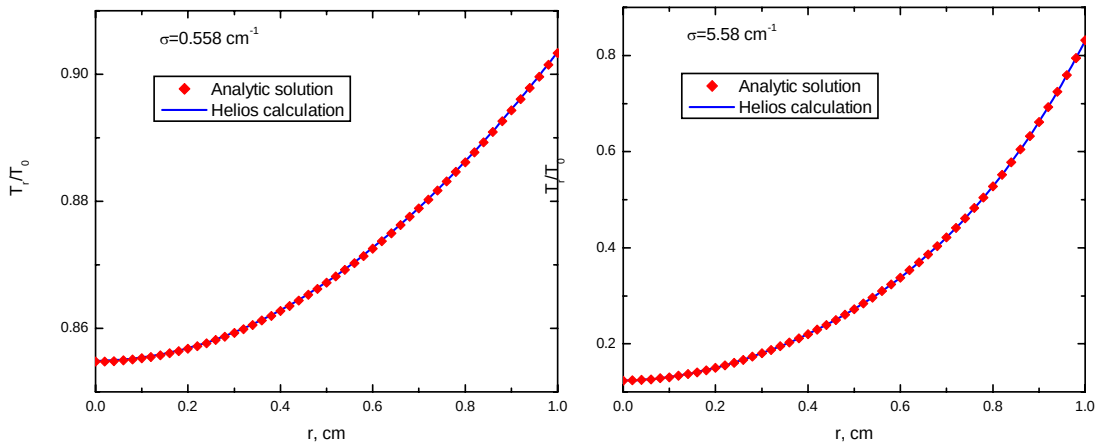

Figure 4. Comparison between steady-state analytic solutions (red symbols) and HELIOS diffusion model results (blue curve) for a uniform cylindrical plasma. Results are shown for σ = 0.558 cm^{-1} in the left plot, and σ = 5.58 cm^{-1} in the right plot. Note that the analytic solution for diffusion does not include flux limiting.

Applications

As a practical application of the radiation transport models in *HELIOS*, the simulation of radiation propagation through gold (Au) and plastic (CH) planar slabs are shown below. Results from the Au simulations are compared with data obtained from NOVA cylindrical hohlraum experiments (Porter et al., LLNL ICF Quarterly Report, UCRL-LR-105821-94-4 (1994)).

In each simulation, the slab is exposed to a time-dependent radiation field on one side. The radiation field is assumed to be Planckian, with estimates for the radiation (or "drive") temperature constrained by experimental DANTE measurements of Porter et al. The assumed drive temperature is shown in Figure 5.

Figure 5. Radiation drive temperature used in Au and CH radiation burnthrough examples.

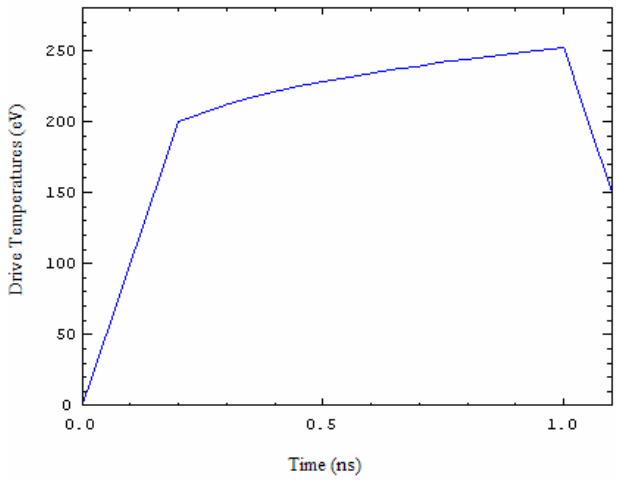

For the material properties in these simulations, PROPACEOS (PRism OPACity and Equation Of State) multigroup opacities were used, along with SESAME equations of state.

Case 1. Au Radiation Burnthrough

Results from *HELIOS* simulations for 1 and 2 μm-thick Au foils are shown in Figure 6. Here the radiation flux emitted from the rear side of the foil is shown as a function of time. Results are shown from calculations using the multi-angle short characteristics model (solid squares) and the flux-limited diffusion model (open circles).

Note that for these Au simulations, the differences in the results for the multi-angle and diffusion cases are small. This is because high-Z materials such as Au have relatively high opacities and short photon mean free paths. Under these circumstances, assumptions in the diffusion approximation are valid.

Figure 7 shows the radiation burnthrough data obtained from the NOVA experiments of Porter *et al.* (1994). Comparing Figures 6 and 7, it is seen that the simulations are in good agreement with the experimental data for both the 1 μm-thick and 2 μm-thick cases.

Figure 6. Calculated flux at the rear surface of 1 and 2 μm-thick Au foils. Results are shown from simulations using the multi-angle (solid squares) and diffusion (open circles) radiation transport models.

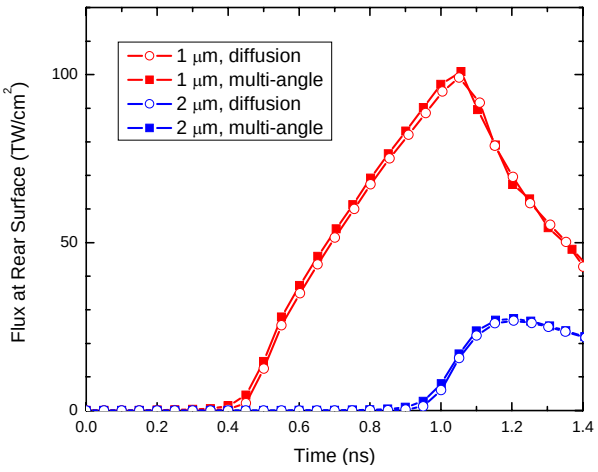

Figure 7. Streak camera data recording the burnthrough of radiation at the rear surface of 1 and 2 μm-thick Au foils (from Porter *et al.*, 1994).

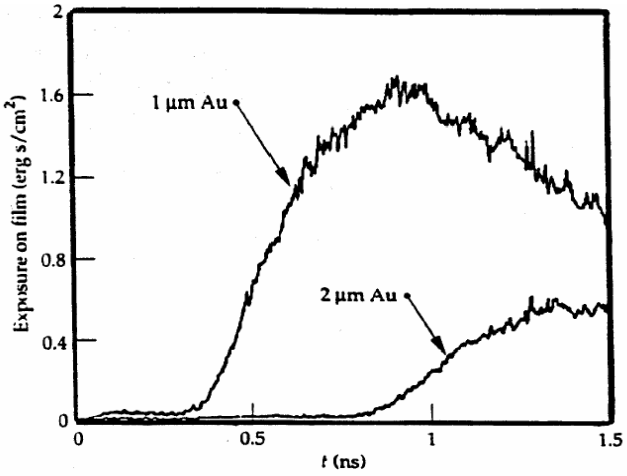

Case 2. CH Radiation Burnthrough

Results from *HELIOS* simulations for 10 μm-thick CH foils are shown in Figure 8. Again, the radiation flux emitted from the rear side of the foil is shown as a function of time. Results are shown from calculations using the multi-angle short characteristics model (solid squares) and the flux-limited diffusion model (open circles).

Unlike the Au case, the CH simulations show significant differences between results using the multi-angle and diffusion radiation transport models. This is because of the lower opacities for the (low-Z) CH, which makes the diffusion approximation less applicable (see, *e.g.*, G. Rochau, Ph.D. Dissertation, Dept. of Engineering Physics, Univ. of Wisconsin (2003)).

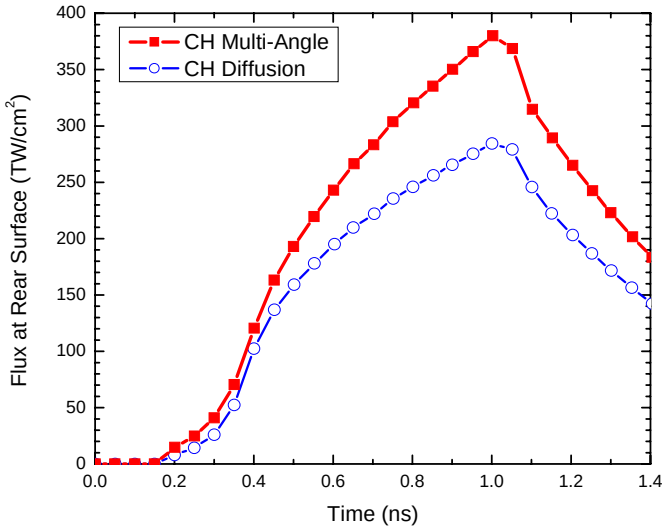

Figure 8. Calculated flux at the rear surface of a 10 μm-thick CH planar slab. Results are shown from simulations using the multi-angle (solid squares) and diffusion (open circles) radiation transport models.